Quantitative Defect Size Evaluation in Fluid-Carrying Nonmetallic Pipes

Maharshi B. Shah, *Graduate Student Member, IEEE*, Yuki Gao, *Member, IEEE*, Maryam Ravan, *Senior Member, IEEE*, and Reza K. Amineh, *Senior Member, IEEE*

***Abstract*— There is a rapid trend in various industries to replace the metallic pipes by nonmetallic ones. This is due to the certain properties, such as high strength, lightweight, resilience to corrosion, and low cost of maintenance for nonmetallic pipes. Despite the abovementioned advantages, nonmetallic pipes are still affected by issues, such as erosion, defects, damages, cracks, holes, delamination, and changes in the thickness. These issues are typically caused due to the manufacturing process, type of carried fluid composition, and flow rate. If not examined well, these issues could lead to disastrous failures caused by leakages and bursting of the pipes. To prevent such major failures, it is extremely important to test the pipes periodically for an accurate estimation of their thickness profile. In this article, we propose a nondestructive testing (NDT) technique, based on near-field microwave holography, for identifying the fluid carried by a nonmetallic pipe and estimating the pipe's thickness profile. Identifying the carried fluid helps improve the thickness profile estimation. The performance of the proposed techniques will be demonstrated via simulations and experiments.**

***Index Terms*— Microwave imaging, millimeter wave imaging, near-field holography, nondestructive testing (NDT), nonmetallic pipes.**

I. Introduction

NOWADAYS, industrial pipes made with nonmetallic materials are rapidly replacing the metallic ones. Fiber reinforced plastic (FRP), glass reinforced epoxy resin (GRE), high-density polyethylene (HDPE), reinforced rubber expansion joints (REJs), carbon FRPs (CFRPs), and polyvinyl chloride (PVC) are some examples of nonmetallic materials used for making the pipes. The growing use of these materials is due to certain properties, such as durability, lightweight, resilience to corrosion, and low cost of maintenance. Despite these advantages, erosion, defects, damages, cracks, holes, delamination, and changes in thickness can lead to leakages and bursting of the pipes. Thus, nondestructive testing (NDT) methods are required for periodic testing of nonmetallic pipes to detect and repair the abovementioned issues [1], [2]. Historically, various successful NDT techniques have been developed mainly for detection and localization of the buried nonmetallic pipes. For a comprehensive review, please refer to [3]. However, in this article, we focus on the assessment of the defects on the pipe. In the following, we first review various NDT techniques for nonmetallic pipe evaluation and then discuss our proposed methodology.

Ultrasonic testing is a commonly used NDT method for testing nonmetalic materials. This testing method fails for composite materials, such as FRP/GRE and HDPE, due to the structure complexity and type of defects [4]–[8]. Radiography, which uses X-ray, is another method applied for such testing, but it requires additional safety and cannot detect defects for which the local density remains approximately constant [9].

Microwave measurement techniques have been employed to solve the problems faced by traditional ultrasonic and radiography NDT testing for inspection of the nonmetallic components (see [10], [11]). There are two groups of microwave sensing techniques for such applications: sensing or imaging based on the raw responses and imaging based on the synthetic aperture radar (SAR) processing.

For the first group, several near-field layered structure inspection techniques have been developed using microwave and millimeter waves (see [12]–[14]). Although very accurate (in fraction of mm range) thickness estimations have been provided in these works, they lack further postprocessing to provide high resolution thickness profile estimation along the cross-range direction. More recently, a line crawling robot transmitting within the frequency range of 18–26.5 GHz (K-band) has been used to apply microwave reflectometry system and provide images of cracks within HDPE pipes [15]. Furthermore, in [16]–[19], 2-D imaging has been performed using only scalar measurements.

As for the second group (SAR imaging), here, we focus on the works related to the nonmetallic pipe imaging. In [20], wideband millimeter wave SAR imaging has been employed along with a low-cost portable single antenna reflectometer operating in Ka-band (26.5–40 GHz). This method generates multiple 3-D images of defects within curved and flat HDPE pipes. In [21], an X-band (8.2–12.4 GHz) SAR imaging has been employed for NDT of multilayered pipes. There, an image reconstruction process is based on the use of matched filters. In [22], an NDT process has been proposed for symmetric and asymmetric layered cylindrical lossy dielectric objects. The technique is based on the time reversal SAR imaging in X-band (8.2–12.4 GHz) while considering the transmission and refraction path at the boundaries between

Manuscript received March 6, 2022; revised May 3, 2022; accepted May 10, 2022. This work was supported in part by the U.S. National Science Foundation (NSF) under Award 1920098 and in part by the New York Institute of Technology's Institutional Support for Research and Creativity (ISRC) Grants. *(Corresponding author: Reza K. Amineh.)*

The authors are with the Department of Electrical and Computer Engineering, New York Institute of Technology, New York, NY 10023 USA (e-mail: rkhalaja@nyit.edu).

Color versions of one or more figures in this article are available at https://doi.org/10.1109/TMTT.2022.3176904.

Digital Object Identifier 10.1109/TMTT.2022.3176904

different layers. In [23], an algorithm has been proposed based on autofocus range-Doppler and singular value decomposition to attenuate the effect of the insulation layer and improve the SAR imaging for insulated steel pipes using X-band (8.2–12.4 GHz), Ku-band (12.4–18 GHz), and K-band (18–26.5 GHz). Overall, the resemblance between SAR-based imaging and direct holographic imaging is well understood as explained in [24]. Despite being fast and robust, these techniques suffer the following shortcomings. First, assuming analytical forms for the incident field and Green's function limit their performance to far-field imaging applications. Since they are incapable of processing evanescent wave spectrum, their resolution is diffraction-limited even when part of the evanescent wave spectrum can be measured in extreme near-field imaging applications. Second, transmitting and receiving antennas are assumed to be pointwise while this assumption contributes to further errors in near-field imaging applications. Third, exact dielectric properties of the background medium need to be known *a priori* to use them in the relevant incident field and Green's function expressions.

To overcome the drawbacks described earlier, an extension of the holographic imaging for near-field applications, referred to as near-field holographic imaging, has been proposed for 2-D [25] and 3-D [26]–[28] imaging. In particular, in [29] and [30], a method has been proposed to obtain Green's function and incident field information for a specific imaging system by measuring the point-spread function (PSF) of the system. In [31], near-field microwave holographic imaging has been proposed for inspection of multiple concentric nonmetallic pipes. Therefore, a standardized minimum norm approach has been employed to mitigate the depth biasing problem. To reduce the complexity of the system, narrowest possible frequency band has been employed using an array of receiver antennas.

Here, the near-field holographic processing is extended further to provide thickness profile estimation for a single thick pipe. Unlike the technique in [31], which provides qualitative images of double pipes, here, using the striking range (radial) resolution achieved when using arrays of receiver antennas scanning a circular aperture, we derive a method to reconstruct the thickness profile (quantitative image) of the pipe along the azimuthal direction. Although the theory and the results presented here are for 1-D imaging (along the azimuthal direction only), extension of the method to include the other cross-range direction, namely, the longitudinal direction, is straightforward (please refer to [31]). Furthermore, a novel technique is presented to identify the type of fluid carried by the pipe along with the thickness profile estimation. Identifying the carried fluid results in reducing the errors in thickness estimations. While preliminary results related to the proposed techniques have been presented in [32], here, we provide a comprehensive study of the effect of main parameters on the thickness profile estimations via simulations and experiments.

II. Theory

Here, we first review the theory of near-field holographic processing in a cylindrical setup, with an array of receiver antennas and multiple frequency data (preferably over a narrowband to reduce the cost and complexity of the system). In [33], we have demonstrated that, using single frequency or narrowband frequency data provided by an array of receiver antennas, striking resolution can be achieved along the radial direction. Here, we first review the theory of near-field holographic processing using an array of receiver antennas and then proceed toward derivation of the thickness profile estimation and fluid-type identification.

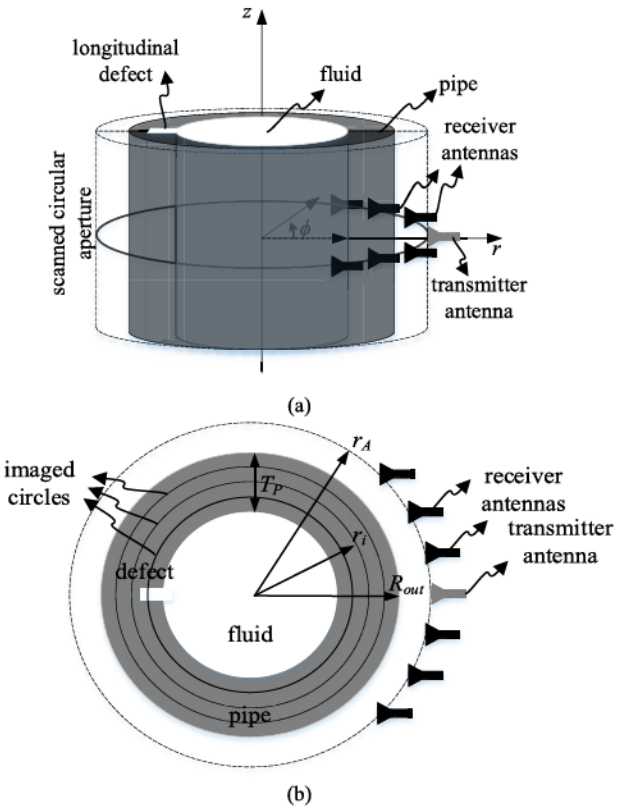

Fig. 1. Illustration of the microwave imaging setup. (a) Transmitter antenna and an array of receiver antennas scanning the PUT over a full circle. (b) Cross section of the setup.

A. Near-Field Holographic Imaging of a Thick Pipe

Fig. 1 illustrates the setup including a transmitter antenna to illuminate the pipe under test (PUT) and an array of N_A receivers antennas that scan the scattered fields. The pipe has a thickness of T_P and an outer radius of R_{out}. The transmitter antenna and the array of receiver antennas scan a circular aperture with a radius of r_A. The antennas rotate altogether over a full circle along the azimuthal direction ϕ at N_ϕ evenly distributed angles.

The complex-valued scattered field, $E^{\text{SC}}(\phi)$, is measured, at each sampling position, at N_ω frequencies within the band of ω_1 to ω_{N_ω}, by each receiver antenna. This complex-valued scattered field, $E^{\text{SC}}(\phi)$, is then calibrated by subtracting the responses without the presence of the defects, namely, the background responses, from the responses when the defects are present. In practice, the responses obtained in regions far away from the defects can be employed as the background responses. The technique then provides 1-D images over N_r

circles with radii $r_i = R_{\text{out}} - T_P + T_P(2i-1)/(2N_r)$, where $i = 1, \ldots, N_r$ and $(R_{\text{out}} - T_P) < r_i < R_{\text{out}}$, as described in the following.

The imaging system is assumed to be linear and space-invariant (LSI), which indicates the use of Born approximation for the scattering integral [26]. First, the PSFs of the LSI system are acquired approximately by measuring small defects, called pointwise defects (PDs), placed over imaged circles one at a time. These responses are then calibrated, as discussed earlier. The calibrated PSF recorded for a PD placed on the ith circle measured by the a_mth receiver ($a_m = 1, \ldots, N_A$) at frequency ω_n is denoted by $E^{\text{SC,PD}}_{i,a_m}(\phi, \omega_n)$. According to [31], the response due to the defects on all the imaged circles, $E^{\text{SC}}_{a_m}(\phi, \omega_n)$, is obtained as

$$E^{\text{SC}}_{a_m}(\phi, \omega_n) = \sum_{i=1}^{N_r} E^{\text{SC,PD}}_{i,a_m}(\phi, \omega_n) \overset{\star}{_\phi} f_i(\phi) \tag{1}$$

where $\overset{\star}{_\phi}$ denotes the convolution operator along the ϕ-axis, and $f_i(\phi)$ denotes the defects' contrast function on imaged circle $r = r_i$. This contrast function depends on the wavenumbers of the defected region and the pipe. In (1), PSF functions, $E^{\text{SC,PD}}_{i,a_m}(\phi, \omega_n)$, can be obtained *a priori* via measurements. Besides, $E^{\text{SC}}_{a_m}(\phi, \omega_n)$ is obtained by calibrating the recorded responses for the defected PUT.

Let us first consider the spatially sampled versions of $E^{\text{SC}}_{a_m}(\phi, \omega_n)$, $E^{\text{SC,PD}}_{i,a_m}(\phi, \omega_n)$, and $f_i(\phi)$ denoted by $\mathbf{E}^{\text{SC}}_{a_m}(n_\phi, \omega_n)$, $\mathbf{E}^{\text{SC,PD}}_{i,a_m}(n_\phi, \omega_n)$, and $\mathbf{f}_i(n_\phi)$, $n_\phi = 1, \ldots, N_\phi$, with angular interval denoted by $\Delta\phi$. Considering the periodicity of the functions along the ϕ-direction, the discrete time Fourier transforms (DTFTs) for the N_ϕ-periodic sequences along ϕ are computationally reduced to discrete Fourier transforms (DFTs) of these sequences [34]. The DFTs with respect to the ϕ variable for sequences $\mathbf{E}^{\text{SC}}_{a_m}(n_\phi, \omega_n)$, $\mathbf{E}^{\text{SC,PD}}_{i,a_m}(n_\phi, \omega_n)$, and $\mathbf{f}_i(n_\phi)$ are denoted by $\tilde{\mathbf{E}}^{\text{SC}}_{a_m}(k_\phi, \omega_n)$, $\tilde{\mathbf{E}}^{\text{SC,PD}}_{i,a_m}(k_\phi, \omega_n)$, and $\tilde{\mathbf{f}}_i(k_\phi)$, where k_ϕ is an integer from 0 to $N_\phi - 1$. Equation (1) can be written as

$$\tilde{\mathbf{E}}^{\text{SC}}_{a_m}(k_\phi, \omega_n) = \sum_{i=1}^{N_r} \tilde{\mathbf{E}}^{\text{SC,PD}}_{i,a_m}(k_\phi, \omega_n) \tilde{\mathbf{f}}_i(k_\phi). \tag{2}$$

When meausirng the responses at all the frequencies and for all the receivers, a system of equations can be constructed at each Fourier variable k_ϕ as

$$\underline{\tilde{\mathbf{E}}}^{\text{SC}} = \underline{\underline{\tilde{\mathbf{D}}}}\, \underline{\tilde{\mathbf{F}}} \tag{3}$$

where

$$\underline{\tilde{\mathbf{E}}}^{\text{SC}} = \begin{bmatrix} \underline{\tilde{\mathbf{E}}}^{\text{SC}}_1 \\ \vdots \\ \underline{\tilde{\mathbf{E}}}^{\text{SC}}_{N_A} \end{bmatrix}, \quad \underline{\underline{\tilde{\mathbf{D}}}} = \begin{bmatrix} \underline{\underline{\tilde{\mathbf{D}}}}_1 \\ \vdots \\ \underline{\underline{\tilde{\mathbf{D}}}}_{N_A} \end{bmatrix}, \quad \underline{\tilde{\mathbf{F}}} = \begin{bmatrix} \tilde{\mathbf{f}}_1(k_\phi) \\ \vdots \\ \tilde{\mathbf{f}}_{N_r}(k_\phi) \end{bmatrix} \tag{4}$$

and

$$\underline{\tilde{\mathbf{E}}}^{\text{SC}}_{a_m} = \begin{bmatrix} \tilde{\mathbf{E}}^{\text{SC}}_{a_m}(k_\phi, \omega_1) \\ \vdots \\ \tilde{\mathbf{E}}^{\text{SC}}_{a_m}(k_\phi, \omega_{N_\omega}) \end{bmatrix} \tag{5}$$

$$\underline{\underline{\tilde{\mathbf{D}}}}_{a_m} = \begin{bmatrix} \tilde{\mathbf{E}}^{\text{SC,PD}}_{1,a_m}(k_\phi, \omega_1) & \cdots & \tilde{\mathbf{E}}^{\text{SC,PD}}_{N_r,a_m}(k_\phi, \omega_1) \\ \vdots & \ddots & \vdots \\ \tilde{\mathbf{E}}^{\text{SC,PD}}_{1,a_m}(k_\phi, \omega_{N_\omega}) & \cdots & \tilde{\mathbf{E}}^{\text{SC,PD}}_{N_r,a_m}(k_\phi, \omega_{N_\omega}) \end{bmatrix}. \tag{6}$$

These systems of equations are solved at each spatial frequency variable k_ϕ to estimate the images in the Fourier domain $\widehat{\tilde{\mathbf{f}}}_i(k_\phi)$, $i = 1, \ldots, N_r$. Then, inverse DFT along azimuthal direction ϕ is applied to reconstruct 1-D images, $\widehat{\mathbf{f}}_i(n_\phi)$, $i = 1, \ldots, N_r$. At the end, the normalized modulus of $\widehat{\mathbf{f}}_i(n_\phi)$, $|\widehat{\mathbf{f}}_i(n_\phi)|/M$, where M is the maximum of $|\widehat{\mathbf{f}}_i(n_\phi)|$ for all r_i, is plotted versus ϕ to obtain a 1-D image of the defects on the ith circle. We call $|\widehat{\mathbf{f}}_i(n_\phi)|/M$ the normalized image.

Recently, it has been shown in [31] that using standardization of the minimum norm inverse solution leads to better results compared with the conventionally used minimum norm solution when processing the data from an array of receiver antennas in near-field holographic imaging. Thus, the standardized estimate of $\tilde{\mathbf{F}}$ can be obtained as [31]

$$\underline{\widehat{\tilde{\mathbf{F}}}} = \sqrt{\left(\text{Diag}\left(\underline{\underline{\mathbf{S}}}_{\underline{\widehat{\tilde{\mathbf{F}}}}}\right)\right)^{-1}}\, \underline{\underline{\mathbf{P}}}\, \underline{\tilde{\mathbf{E}}}^{\text{SC}} \tag{7}$$

where

$$\underline{\underline{\mathbf{S}}}_{\underline{\widehat{\tilde{\mathbf{F}}}}} = \underline{\underline{\tilde{\mathbf{D}}}}^H \left(\underline{\underline{\tilde{\mathbf{D}}}}\, \underline{\underline{\tilde{\mathbf{D}}}}^H + \alpha \underline{\underline{\mathbf{L}}}\right)^+ \underline{\underline{\tilde{\mathbf{D}}}} \tag{8}$$

$$\underline{\underline{\mathbf{P}}} = \underline{\underline{\tilde{\mathbf{D}}}}^H \underline{\underline{\mathbf{L}}} \left[\underline{\underline{\mathbf{L}}}\, \underline{\underline{\tilde{\mathbf{D}}}}\, \underline{\underline{\tilde{\mathbf{D}}}}^H \underline{\underline{\mathbf{L}}} + \alpha \underline{\underline{\mathbf{L}}}\right]^+ \tag{9}$$

$$\underline{\underline{\mathbf{L}}}_{N_\omega N_A \times N_\omega N_A} = \underline{\underline{\mathbf{I}}} - \underline{\mathbf{1}}\, \underline{\mathbf{1}}^T / \underline{\mathbf{1}}^T \underline{\mathbf{1}} \tag{10}$$

where $\underline{\underline{\mathbf{I}}}_{N_\omega N_A \times N_\omega N_A}$ is the identity matrix, $\underline{\mathbf{1}}_{N_\omega N_A \times 1}$ is a vector of ones, $[\cdot]^H$ is the Hermitian transpose operation, $[\cdot]^+$ denotes the Moore–Penrose pseudoinverse, $\alpha \geq 0$ is a regularization parameter, and $\text{Diag}(\underline{\underline{\mathbf{S}}}_{\underline{\widehat{\tilde{\mathbf{F}}}}})$ is the diagonal matrix formed by the diagonal elements of $\underline{\underline{\mathbf{S}}}_{\underline{\widehat{\tilde{\mathbf{F}}}}}$.

B. Pipe's Thickness Estimation

In [31], when imaging double concentric pipes, we have shown that excellent radial (range) resolution can be obtained because of the near-field nature of the imaging technique. Here, we exploit this characteristic to implement a quantitative evaluation of a single pipe's thickness. Rather than only providing the 1-D images, we proceed to provide an estimation of the thickness of the pipe at various angular positions. This helps to estimate the material loss due to the defects. For this purpose, first, we reconstruct 1-D images along the ϕ-axis as explained in Section II-A. Then, we combine these qualitative images, as follows, to obtain a quantitative estimation of the thickness variation along the ϕ-axis $T(n_\phi)$:

$$T(n_\phi) = T_P \left(1 - \frac{1}{N_r} \sum_{i=1}^{N_r} \frac{\left|\widehat{\mathbf{f}}_i(n_\phi)\right|}{M}\right). \tag{11}$$

In fact, this works by applying superposition of the effects of the defect on all the imaged circles. The effect due to larger defects along the radial direction will be observed on a larger number of imaged circles, in turn, leading to larger deviation from the nominal thickness.

C. Fluid Identification Approach

So far, we have assumed that the type (properties) of the fluids carried inside the pipe is exactly known. However, in practice, there might be uncertainty in knowing the fluid, which leads to thickness estimation errors. To estimate the fluid type, we propose an approach with the following steps.

1) Divide the responses acquired by all the N_r receivers (RX_i, where $i = 1, \ldots, N_r$) into two sets: Set 1 includes responses corresponding to the receivers RX_o, where o is an odd integer number, and Set 2 includes responses corresponding to the receivers RX_e, where e is an even integer number.
2) Guess N_f number of possible fluids carried by the pipe and measure the PSFs related to these fluids *a priori*.
3) For each assumed fluid identified by number $n_f = 1, \ldots, N_f$, we use Set 1 and Set 2 responses corresponding to the relevant PSFs and PUT scenarios and apply holographic algorithm on them separately to obtain the estimated thicknesses, $T_1^{n_f}(n_\phi)$ and $T_2^{n_f}(n_\phi)$, respectively.
4) For each assumed fluid in Step 3, the difference between the estimated thicknesses $T_1^{n_f}(n_\phi)$ and $T_2^{n_f}(n_\phi)$ is evaluated as

$$\Delta T(n_f) = \left|\left| T_1^{n_f}(n_\phi) - T_2^{n_f}(n_\phi) \right|\right| \tag{12}$$

where $||\cdot||$ is the two-norm operator.
5) The true fluid carried by the pipe is identified as the one for which ΔT is the lowest. This indicates that the estimated thicknesses obtained from Set 1 and Set 2 responses are the most consistent when they are computed with the PSF corresponding to the right fluid.

Fig. 2 shows the flowchart of the algorithm summarizing the abovementioned steps. Once the fluid type is identified, responses from both sets and the PSFs corresponding to the identified fluid are employed for the final thickness estimation.

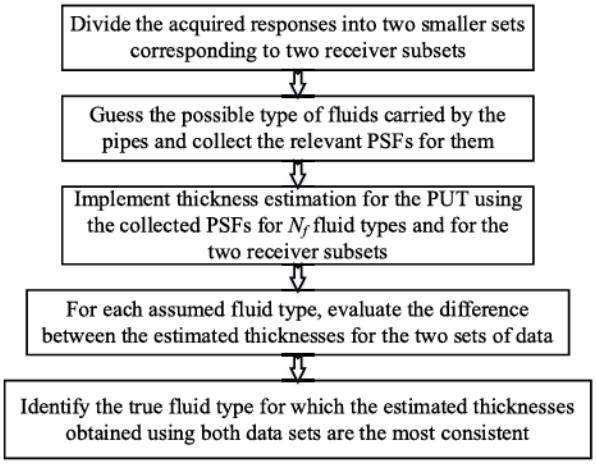

Fig. 2. Flowchart of pipe's fluid-type identification.

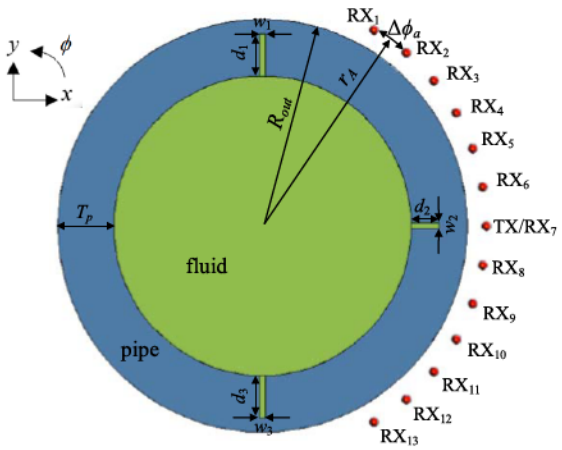

Fig. 3. Illustration of FEKO simulation setup consisting of an array of 13 antennas with angular separation of $\Delta\phi_a$ scanning outside the pipe at radius of r_A and along the azimuthal direction. The pipe has an outer radius of R_{out} and a thickness of T_P. The pipe has three defects centered at $\phi = -90°$, 0°, and 90°. The pipe carries a fluid, which is a mixture of 20% water and 80% glycerin.

III. Simulation Results

To study the performance of the proposed thickness estimation technique, here, we conduct a simulation study based on the use of Feldberechnung für körper mit beliebiger oberfläche (FEKO) software. To have a realistic simulation study, white Gaussian noise with signal-to-noise ratio (SNR) of 20 dB is added to the data using the *awgn* command in MATLAB. Besides, to evaluate the quality of the thickness estimation, we define the total percentage of estimation error E_T as

$$E_T = \sum_{i=1}^{N_r} \frac{\left\| T(n_\phi) - T_{\text{true}}(n_\phi) \right\|}{\left\| T_{\text{true}}(n_\phi) \right\|} \times 100 \tag{13}$$

where $T_{\text{true}}(n_\phi)$ is the true thickness profile of the pipe. The computed values of E_T will be presented on top of each relevant figure.

A. Simulation Model

In the simulation setup, we use an array of 13 resonant dipole antennas, as illustrated in Fig. 3, separated by $\Delta\phi_a = 10°$ along the ϕ-direction (azimuth angle) and scanning at $r_A = 80$ mm from the center. The center element is excited while all the antennas are used as the receivers. In FEKO, we perform the scanning of a circular aperture to get the complex-valued S-parameters by rotating the antenna(s) along the azimuth angle (ϕ) from 0° to 360° in 181 grid points (every 2°). The outer radius and the thickness of the pipe are $R_{\text{out}} = 73$ mm and $T_P = 20$ mm, respectively. There are three defects on the pipe centered at $\phi = -90°$, 0°, and 90° as shown in Fig. 3 with the parameters of the defects as $w_1 = w_2 = w_3 = 2$ mm, $d_1 = d_3 = 15$ mm, and $d_2 = 10$ mm. Table I shows the values of the parameters for this setup. The pipe is assumed to be polyethylene with a relative permittivity ε_r of 2.25 and a loss tangent of 0.0004. The pipe carries a mixture of 20% water and 80% glycerin with properties obtained from [35] and presented in Table II.

To estimate the pipe's thickness profile, holographic imaging is applied to obtain 1-D images over $N_r = 4$ circles with the radii of $r_i = R_{\text{out}} - T_P + T_P(2i-1)/(2N_r)$, where

TABLE I

PARAMETER VALUES FOR THE SETUP IN FIG. 3

N_A	$\Delta\phi_a$	r_A	R_{out}	T_P	ε_r	tanδ	fluid
13	10°	80 mm	73 mm	20 mm	2.25	0.0004	20% water and 80% glycerin

TABLE II

ELECTRICAL PROPERTIES OF MIXTURE OF 20% WATER AND 80% GLYCERIN OBTAINED FROM [35]

Frequency (GHz)	ε_r	σ (S/m)
1	22	1.25
7	10	4
13	7	5

$i = 1, \ldots, N_r$. For this purpose, first, the PSFs corresponding to these four imaged circles are simulated. This is performed by placing PDs, with the dimensions of 5 and 2 mm along the radial and azimuthal directions, respectively, over each circle one at a time and simulate the responses. Then, the scattered responses (for PSFs and defect responses) are calibrated using the simulated background responses obtained by scanning the PUT without any defects. Finally, the proposed thickness estimation method is applied on the calibrated scattered responses.

B. Quantitative Analysis and Feature-Based Evaluation

Here, we provide an analysis of the effect of parameters, such as frequency, number of receivers, crack width, standoff distance, and antenna separation. We also compare the raw response obtained from a single waveguide against the thickness profile estimated with the proposed method.

Fig. 4 shows the estimated thickness of the pipe when using only single frequency data at 1, 7, and 13 GHz. It is observed that the accuracy of the thickness estimation improves (E_T decreases) with the increase in the operation frequency. This is mainly due to better resolutions at higher frequencies. For example, at 1 GHz, the sizes of the defects along the radial direction are overestimated. We continue implementing further investigations with the operation frequency of 7 GHz, which allows for a compromise between the cost of data acquisition circuitry and resolution.

Then, we study the effect of number of receivers used for thickness estimation. For this purpose, we leave out the data for some of the receivers when employing operation frequency of 7 GHz in the previous example. Fig. 5 shows the estimated thickness profiles when we employ seven receiver antennas (RX1, RX3, RX5, RX7, RX9, RX11, and RX13), five receiver antennas (RX1, RX4, RX7, RX10, and RX13), three receiver antennas (RX1, RX7, and RX13), and three receiver antennas (RX6, RX7, and RX8). It is observed that the total error E_T in thickness profile estimation increases with the decrease in the number of utilized receiver antennas, as expected.

Furthermore, we study the quality of thickness profile estimations for cracks with the various widths (w) of 0.5, 1, and 2 mm while keeping the thickness the same as the small crack in Fig. 3. For this purpose, PDs with the dimensions of 5 and 0.1 mm along the radial and azimuthal directions, respectively, are used for collection of PSFs. Fig. 6 shows the thickness profile estimations. It is observed that the estimated thickness deviates from the true thickness as the crack width reduces.

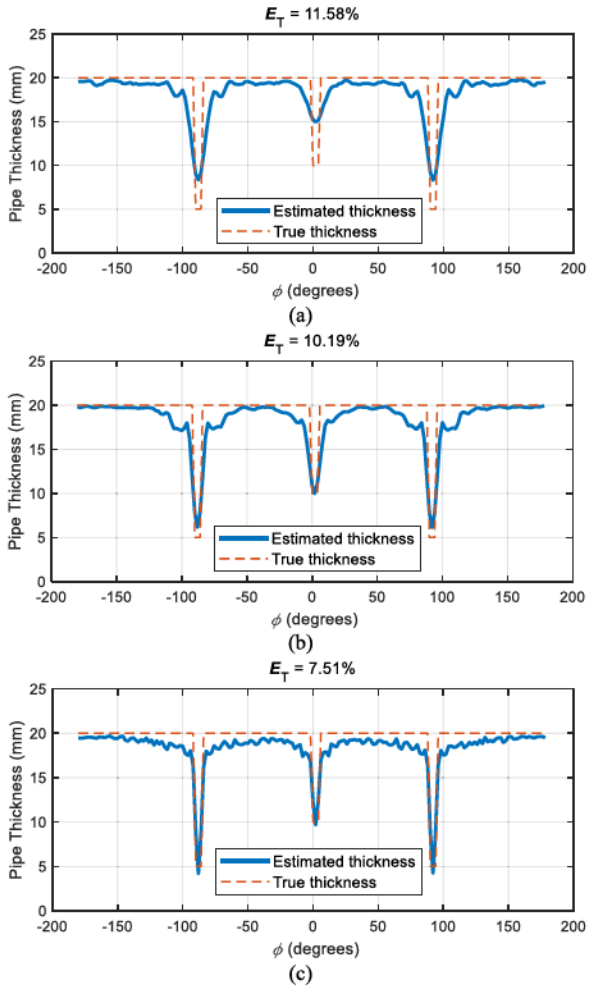

Fig. 4. Estimated thickness profile when using 13 receiver antennas and for operation frequency of (a) 1, (b) 7, and (c) 13 GHz.

Next, we analyze the effect of standoff distance of the antenna array from the outer surface of the pipe. For this purpose, we increase and decrease the original r_A (80 mm) by 0.5 mm for the PUT while the PSFs for the case of $r_A = 80$ mm are employed to evaluate the tolerance of the technique with respect to the change in r_A. Fig. 7 shows the estimated thickness profiles. It is observed that, compared with Fig. 4(b), the estimated thickness profiles deteriorate in both cases. In particular, the estimated nominal thickness deviates from the true 20 mm value with the error in the standoff distance. Besides, the degradation is more when decreasing the value of r_A.

Here, we study the effect of increasing and decreasing the angular separation between the antennas. The original configuration of $\Delta\phi_a = 10°$ is varied by $\pm 2°$. The PSF information is collected with similar modified antenna configurations. Table III shows the values of E_T corresponding to these cases. It is observed that changing $\Delta\phi_a$ has little effect on the estimated thickness profile.

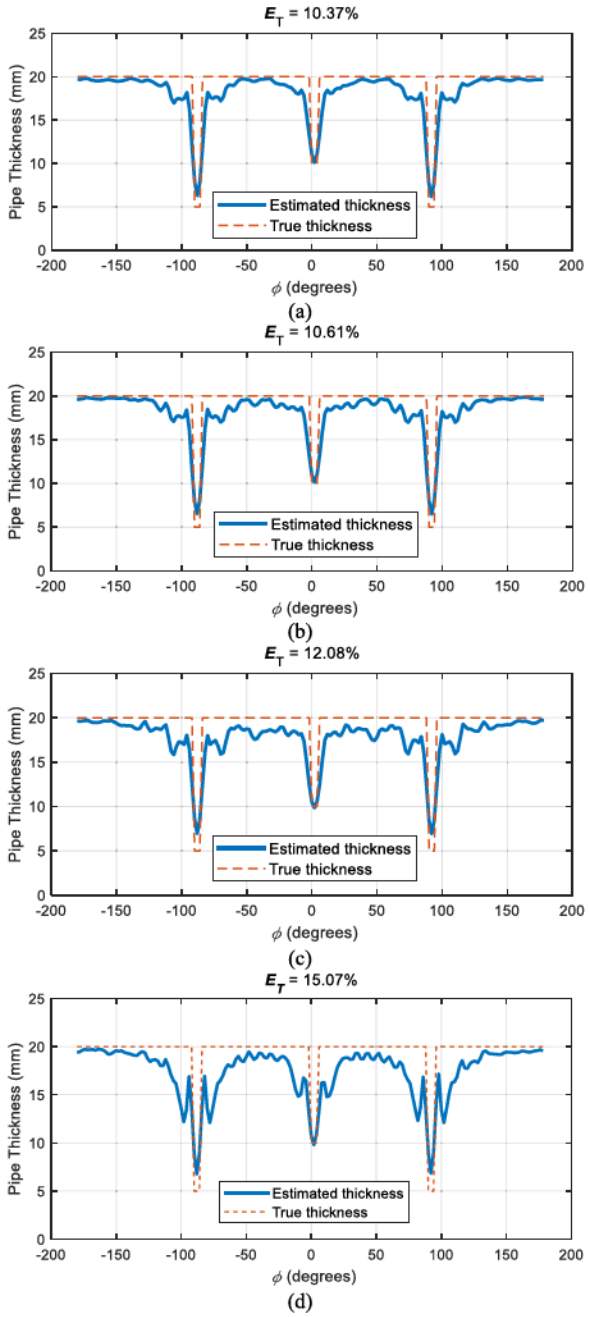

Fig. 5. Estimated thickness profile for configuration in Fig. 3 when using (a) seven receiver antennas (RX1, RX3, RX5, RX7, RX9, RX11, and RX13), (b) five receiver antennas (RX1, RX4, RX7, RX10, and RX13), (c) three receiver antennas (RX1, RX7, and RX13), and (d) three receiver antennas (RX6, RX7, and RX8).

TABLE III
ESTIMATED THICKNESS ERRORS FOR VARIOUS VALUES OF $\Delta\phi_a$ IN FIG. 3

$\Delta\phi_a$ (°)	E_T (%)
8°	10.32%
10°	10.19%
12°	10.44%

To justify the use of the proposed technique, the same pipe is scanned at the operation frequency of 7 GHz by a single rectangular waveguide (WR137 in C-band). Similar as before,

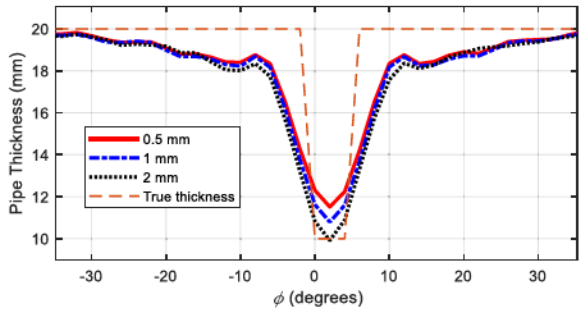

Fig. 6. Comparison of the estimated thicknesses for defects of three different widths (0.5, 1, and 2 mm) and similar thickness as the small defect in Fig. 3.

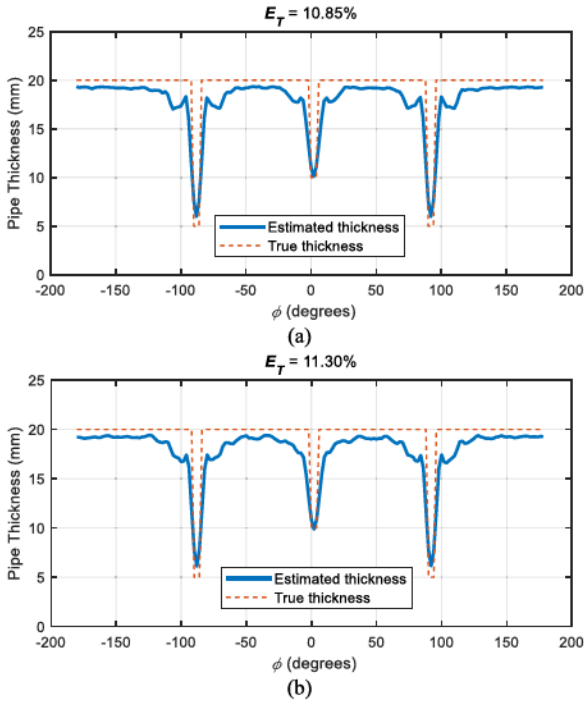

Fig. 7. Estimated thickness profiles at 7 GHz for the defects in Fig. 3 and when (a) increasing r_A by 0.5 mm and (b) decreasing r_A by 0.5 mm.

artificial noise is added to the raw response, and the response is also calibrated. Fig. 8 compares the calibrated raw response for the waveguide with the estimated thickness profile [similar to the one in Fig. 4(b)] and the true thickness profile. It is observed that the waveguide response can show the presence of the defects. However, it suffers poor azimuthal resolution and large levels of artifacts in nondefected regions. Besides, the level of peaks in the calibrated response cannot be clearly correlated with the thickness of the defected regions (the peaks are lower for larger defects). This clearly justifies the need for applying the proposed technique for the thickness profile estimation along the azimuthal direction.

Finally, we performed a feature-based error analysis on the results shown in Figs. 4–7. The three defects positioned at −90°, 90°, and 0° are named $L1$, $L2$, and $S1$, respectively. Table IV shows the thickness estimation error (E_D) for these three defects in addition to summarizing the E_T values for the studied cases. Furthermore, in Section III-D, we present the results of thickness estimation for larger defects.

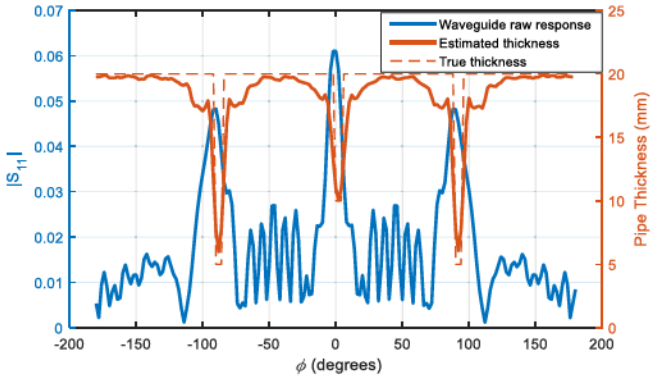

Fig. 8. Comparison of the calibrated raw response obtained from the waveguide scan with the estimated thickness profile and true thickness profile.

TABLE IV
SUMMARY OF ESTIMATION ERRORS

Parameter	Crack	E_T (%)	E_D (%)
1 GHz	{L1, S1, L2}	11.58	{23, 50, 23}
7 GHz	{L1, S1, L2}	10.19	{5.83, 1.5, 5.83}
13 GHz	{L1, S1, L2}	7.51	{4, 2, 4}
RX1, RX3, RX5, RX7, RX9, RX11, RX13	{L1, S1, L2}	10.37	{6.5, 1.5, 6.5}
RX1, RX4, RX7, RX10, RX13	{L1, S1, L2}	10.61	{11.66, 1.5, 11.66}
RX1, RX7, Rx13	{L1, S1, L2}	12.08	{16.5, 2.5, 16.5}
RX6, RX7, RX8	{L1, S1, L2}	15.07	{16.5, 2.5, 16.5}
Defect width {0.5 mm, 1 mm, 2 mm}	S1	10.19	{18, 10, 1}
$r_A = 0.5$ mm	{L1, S1, L2}	11.03	{5.83, 1.5, 5.83}

TABLE V
ELECTRICAL PROPERTIES OF THE MIXTURES OF WATER AND GLYCERIN AT 7 GHZ OBTAINED FROM [35]

glycerin concentration (%)	ε_r	σ (S/m)
55	17	8
62	16	7
70	15	6
75	12	5
80	10	4
85	9	3
90	8	2.5
95	7	2
100	6	1.5

C. Fluid Identification

In this section, we demonstrate the performance of the proposed fluid identification approach. For this purpose, we assume the pipe in the configuration of Fig. 3 could carry mixtures of water and glycerin with unknown glycerin concentrations within the range of 5%–100%. Table V shows the electrical properties of such mixtures obtained from [35].

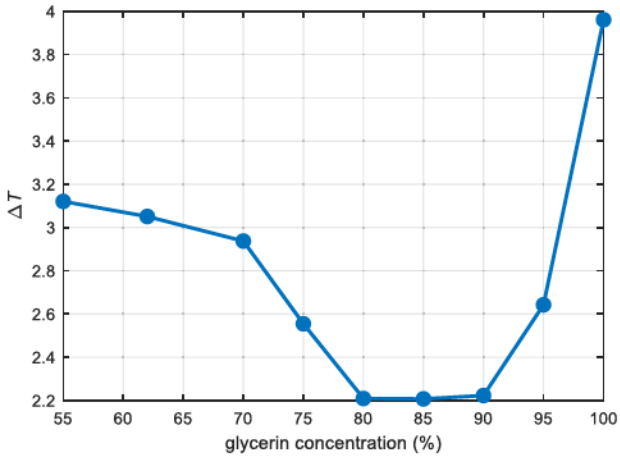

Fig. 9. Variation of ΔT in (12) when using data from two sets of receivers.

First, we collect PSFs for the mixture corresponding to the glycerin concentration of 80% and PDs with the dimensions of 5 and 2 mm along the radial and azimuthal directions, respectively. Then, nine PUT models are simulated with various glycerin concentrations within the range of 55%–100%, as shown in Table V. Having the collected PSFs and the PUT responses, we compute the thickness difference ΔT in (12) for all the PUT models. To implement that, the 13 receivers in Fig. 3 are divided into two subsets as Set 1 containing the responses collected by RX_o where $o = 1, 3, \ldots, 13$ and Set 2 containing the responses collected by RX_e where $e = 2, 4, \ldots, 12$. Fig. 9 shows the computed ΔT values. It is observed that the minimum of ΔT is obtained for the glycerin concentration of 80% for which the PSFs have been employed.

This confirms that the minimum of the ΔT function occurs when the fluid type used in the PSF and the PUT models have electrical properties that are sufficiently close. Once the fluid type is identified, the right PSFs for all the 13 receiver antennas can be employed to obtain the thickness profile estimation with optimal accuracy, as shown in Fig. 4(b).

It is worth noting that, in practice, a database of PSFs for the possible fluid types can be collected *a priori* through measurements, and then, the thickness estimation along with fluid identification procedure can be implemented after collecting the responses for the PUT.

D. Defect's Radial Profile Reconstruction

Here, we study the capability of the proposed technique in radial profile reconstruction of larger defects. For this purpose, we employ the setup shown in Fig. 3, but for a pipe that has a large defect, the profile of that is shown in Fig. 10. Table VI shows the defect parameters. Fig. 11 shows the estimated thickness profile of the pipe. It is observed that the reconstructed thickness profile closely follows the true defect's profile confirming the capability of the proposed technique in reconstructing the shape of the defects.

IV. EXPERIMENTAL RESULTS

In this section, to validate the proposed pipe thickness profile estimation and fluid identification techniques, we conduct proof-of-concept experiments.

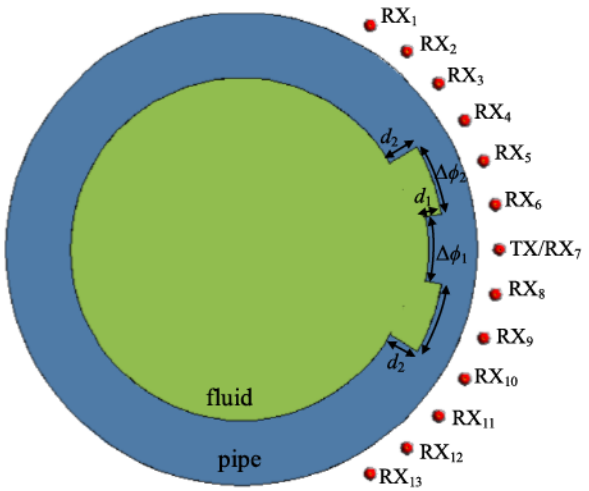

Fig. 10. Illustration of FEKO simulation setup. All the parameters are similar to those presented in Fig. 3 except the defect dimensions.

TABLE VI
PARAMETER VALUES FOR THE DEFECTS IN FIG. 10

d_1	d_2	$\Delta\phi_1$	$\Delta\phi_2$
5 mm	10 mm	20°	20°

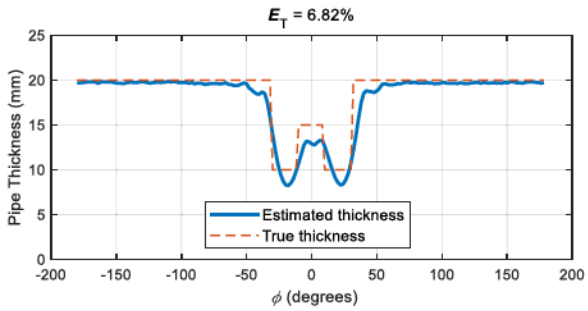

Fig. 11. Estimated thickness profile of the PUT shown in Fig. 10.

TABLE VII
PARAMETER VALUES FOR THE PIPES AND DEFECTS IN FIG. 12

R_{bout}	R_{bin}	R_{yout}	R_{yin}	$\Delta\phi_w$	T_w	$\Delta\phi_s$	T_s
82.5 mm	66.5 mm	66.5 mm	46.5 mm	25°	12 mm	15°	8 mm

A. Pipes, Defects, and Data Acquisition System

For estimating the pipe's thickness at various angular positions (ϕ), we designed and fabricated a two-layer pipe consisting of an outer layer HDPE pipe and an inner layer 3-D printed pipe including retractable defects. Table VII shows the parameter values for the pipes and the defects. The material used for 3-D printing is polylactic acid (PLA). Fig. 12 shows the fabricated two-layer PUT including the HDPE pipe shown in black, the 3-D printed layer seen in yellow, and the 3-D printed retractable pieces to create defects shown in green.

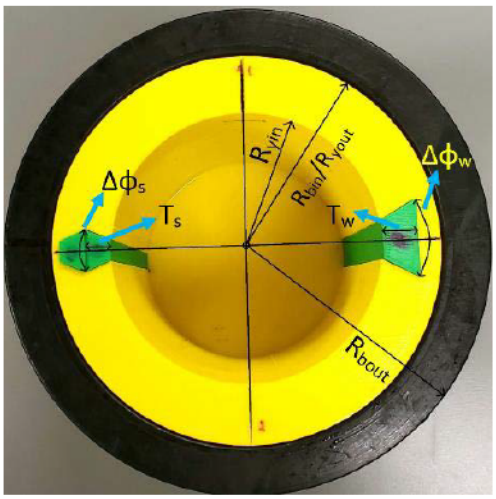

Fig. 12. Fabricated two-layer PUT including HDPE layer seen in black, 3-D printed layer seen in yellow, and 3-D printed retractable pieces to create defects shown in green.

We use an array of 13 2.4-/5.8-GHz dual band 3–3.5-dBi rubber duck dipole antennas manufactured by TAOGLAS [36]. The array of antennas consists of one transmitter antenna, 12 receiver antennas, and microwave absorbing sheets wedged between adjacent antennas. The separation between each antenna along the azimuthal direction is $\Delta\phi_a = 10°$, configured like the simulation study. To alleviate the undesired effect of coupling between these antennas, while they are placed in proximity of each other in the proposed setup, we place microwave absorbing sheets in between them. We have shown in [37] that this leads to higher quality measurements. We employ this antenna array to measure responses at 10 frequencies over 5.5–6.5-GHz band. We first verified that the measured $|S_{11}|$ values for the antennas are mostly below -10 dB over this band while the antennas are inside a 3-D printed holder in contact with the pipes.

The antennas are connected to an RF SP8T switch (EV1HMC321ALP4E) and have an operating frequency up to 8 GHz. The RF switch is controlled via an Arduino Uno board and MATLAB software. We have constructed a cylindrical scanning setup with stepper motors to control the azimuthal movements of the platform on which the PUT is placed. Fig. 13 shows the complete scanning setup when the antenna array supported by the 3-D printed holder is placed outside the PUT.

At each sampling step along the azimuthal direction (in total 100 positions covering 360°), the complex-valued $|S_{21}|$ data are measured by an Anritsu vector network analyzer (VNA) MS46122B for each receiver antenna. The data acquisition including switching between receiver antennas, controlling the scanning system, and VNA measurement is implemented via a single MATLAB code.

B. Pipe Thickness Profile

In the first experiment, the array of antennas scans the PUT filled with 100% water. We assume two levels for thickness estimation of the inner layer (3-D printed layer). For this purpose, we obtain two PSFs, each time, by removing one

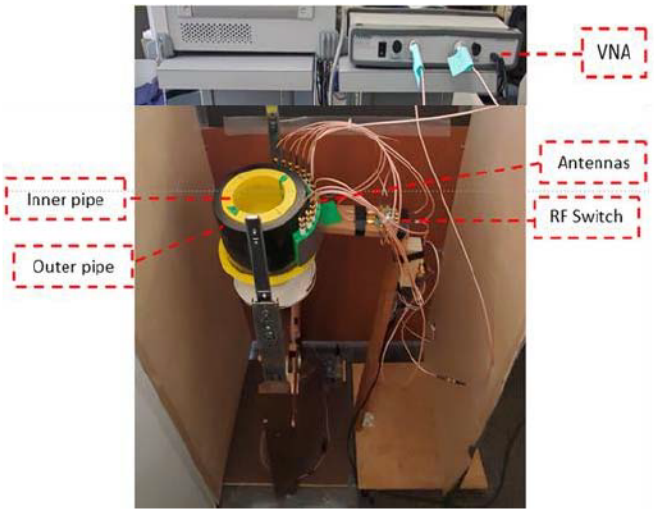

Fig. 13. Experimental setup for thickness estimation of inner pipe in a two-layer pipe configuration.

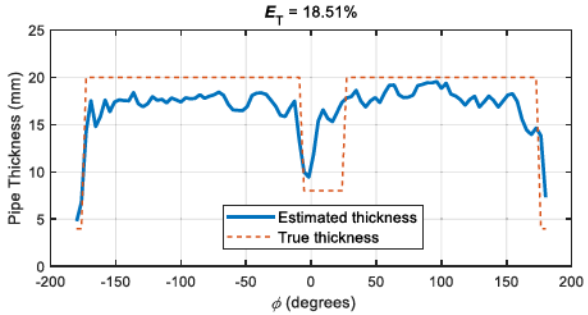

Fig. 14. Estimated thickness profile for the inner layer in Fig. 12.

TABLE VIII
VALUES OF E_T WHEN USING DIFFERENT FREQUENCIES AND ANTENNAS

Parameters	Value	E_T(%)
Utilized Frequencies	6 GHz	30.08
	5.5–6.5 GHz	18.51
No. of Utilized Antennas	6 and 8	21.19
	1 and 13	23.63
	Odd	18.88
	Even	25.29

of the small green pieces on the left-hand side of Fig. 12. Then, we scan the PUT's responses with all the green pieces removed.

Besides, we perform the scan of the PUTs without the presence of any defect (all the green pieces in place) to obtain the background responses for calibrating all the other responses (subtracting the responses without the presence of defects from the responses with the presence of the defects). Fig. 14 shows the estimated thickness profile of the inner layer after applying the technique described in Section II-B.

In the following, we perform further measurement error analysis. As observed from Table VIII, using data at the narrowband of 5.5–6.5 GHz leads to less error compared with using single frequency data at 6 GHz. Besides, the values of E_T when using antenna pairs 6 and 8 (one at each side of the transmitter) are 21.19%, and when using antenna pair

TABLE IX
VARIATION OF ΔT FOR DIFFERENT GLYCERIN CONCENTRATIONS

glycerin concentration (%)	ΔT(%)
0	18.21
20	20.67
40	27.25

farthest from the transmitter, i.e., antennas 1 and 13, are 23.63%. Both these errors are much larger than the error when using the data from all the receiver antennas. Furthermore, as observed in Fig. 8, estimation of the thickness profile is highly influenced by even a small variation of the antenna array's standoff distance; i.e., the estimated nominal thickness deviates from the true value. While performing the PSF and PUT measurements, we always have some unavoidable small random variation of the standoff distance due to our imperfect scanning system. The effect of this variation can be observed as the ripples in the estimated nominal thickness in Fig. 14. This causes the increases in the value of E_T.

C. Fluid Identification

In this section, we perform measurements and show results supporting the performance of the proposed fluid identification approach. For this purpose, we create two additional fluid mixtures including 80% water–20% glycerin and 60% water–40% glycerin.

In this section, we perform measurements and show results supporting the performance of the proposed fluid identification approach. For this purpose, we create two additional fluid mixtures including 80% water–20% glycerin and 60% water–40% glycerin. Then, we collect responses for the defected pipe when removing the larger green piece and for all the three liquid fluids (0% glycerin, 20% glycerin, and 40% glycerin). We calibrate each of the responses by subtracting the corresponding measured background responses. We use the PSFs measured in Section IV-B with 0% glycerin for all three scenarios. Similar to the simulation study, first, the 12 receivers are divided into two subsets as Set 1 containing the responses collected by RX_o where $o = 1, 3, \ldots, 11$ and Set 2 containing the responses collected by RX_e where $e = 2, 4, \ldots, 12$. Then, ΔT values are computed for the measurements with each one of the three liquid fluids.

Table IX shows the variation of ΔT. It is observed that the smallest ΔT is obtained for 0% glycerin for which the correct PSFs have been employed. This confirms that the minimum of the ΔT function occurs when the fluid type used in the PSF and the PUT measurements has very identical electrical properties.

V. CONCLUSION AND DISCUSSION

In this article, we implemented a quantitative thickness estimation of thick nonmetallic pipes. We demonstrated the capabilities of the proposed technique and also studied the effects of important parameters on the thickness profile estimations. We also proposed an approach for fluid-type identification leading to optimal thickness estimations. Furthermore,

we demonstrated the capability of the technique in thickness profile estimation of large defects.

The dipole antennas used in this study offer these benefits: 1) compact size to be used in an array configuration; 2) high sensitivity leading to better dynamic range; 3) relatively low cost; and 4) omnidirectional leading to better resolution in the holographic processing [24].

Furthermore, in general, users are more interested to evaluate common defects such as narrow cracks. In practice, the dynamic range of the measurement system affects the lower limit for the inspected defect size. The dynamic range, in turn, depends on various factors, such as the data acquisition circuitry's noise, ripples in the mechanical scanning, electromagnetic interferences, and so on. One may assume that the accuracy of the thickness estimations will be higher for larger defects. However, larger defects further violate Born approximation used in the proposed technique. This imposes an upper limit on the largest inspected defect size.

Conventionally range resolution is achieved via wideband measurements. However, we have shown in previous works (see [33], [37], [38]) that using an array of receiver antennas scanning single frequency or narrowband data over the measurement aperture (here, [0 to 2π]), allows for achieving excellent range resolution. Here, in the simulation study, we employed single frequency data, which along with the use of receiver arrays allows achieving range (radial) resolution. In experiments, we used narrowband data, which helps improving the thickness estimation results compared with the single frequency data. Utilizing the narrowest frequency band allows for: 1) more cost-effective data acquisition circuitry; 2) reducing the errors due to the dispersion of the materials (normally dispersion is not considered in SAR-based and near-field holographic processing); and 3) utilizing more compact and sensitive (resonant) antennas.

Finally, in the past two decades, various near-field layered-structure microwave NDT techniques have been developed to measure pipe thickness precisely, as discussed in Section I. However, they either lack further postprocessing to provide thickness profile along the cross-range (here, azimuthal) direction or their processing is based on the SAR principles, which cannot process the measured evanescent wave spectrum; i.e., their resolution is diffraction-limited.

REFERENCES

[1] A. Haryono, M. S. U. Rahman, and M. Abou-Khousa, "Inspection of non-metallic pipes using microwave non-destructive testing (NDT)," in *Proc. IEEE Int. RF Microw. Conf. (RFM)*, Dec. 2018, pp. 219–222.

[2] M. S. U. Rahman, A. Haryono, Z. Akhter, and M. A. Abou-Khousa, "On the inspection of glass reinforced epoxy pipes using microwave NDT," in *Proc. IEEE Int. Instrum. Meas. Technol. Conf. (I MTC)*, May 2019, pp. 1–5.

[3] L. Ge *et al.*, "Current trends and perspectives of detection and location for buried non-metallic pipelines," *Chin. J. Mech. Eng.*, vol. 34, no. 1, pp. 1–29, Dec. 2021.

[4] J. Blitz and G. Simpson, *Ultrasonic Methods of Non-destructive Testing*. London, U.K.: Chapman Hall, 1996.

[5] W. M. Alobaidi, E. A. Alkuam, H. M. Al-Rizzo, and E. Sandgren, "Applications of ultrasonic techniques in oil and gas pipeline industries: A review," *Amer. J. Oper. Res.*, vol. 5, no. 4, pp. 274–287, 2015.

[6] L. Tong, A. P. Mouritz, and M. K. Bannister. *3D Fiber Reinforced Polymer Composites*. 1st ed. Oxford, U.K.: Elsevier, 2002.

[7] K. Murphy and D. Lowe, "Evaluation of a novel microwave based NDT inspection method for polyethylene joints," in *Proc. ASME Pressure Vessels Piping Conf.*, Baltimore, MD, USA, Jan. 2011, pp. 321–327.

[8] X. W. Zhu, J. P. Pan, and L. J. Tan, "Microwave scan inspection of HDPE piping thermal fusion welds for lack of fusion defect," *Appl. Mech. Mater.*, vols. 333–335, pp. 1523–1528, Jul. 2013.

[9] R. Pincu, "Digital radiography and its advantages in field NDT inspections today," in *Proc. 17th World Conf. Nondestruct. Test.*, Shanghai, China, Oct. 2008, pp. 25–28.

[10] R. Zoughi, *Microwave Non-Destructive Testing and Evaluation*. Norwell, MA, USA: Kluwer, 2000.

[11] S. Kharkovsky and R. Zoughi, "Microwave and millimeter wave nondestructive testing and evaluation—Overview and recent advances," *IEEE Instrum. Meas. Mag.*, vol. 10, no. 2, pp. 26–38, Apr. 2007.

[12] R. Zoughi and S. Ganchev, "Microwave nondestructive evaluation, state-of-the-art review," in *Prepared for Nondestructive Testing Information Analysis Center*. Austin, TX, USA: Texas Research Institute Austin, Feb. 1995.

[13] R. Felbecker, W. Keusgen, A. Kortke, and M. Peter, "Estimation of effective permittivity and effective thickness of inhomogeneous materials at 52—70 GHz," in *Proc. 3rd Eur. Conf. Antennas Propag. (EuCAP)*, 2009, pp. 3881–3885.

[14] M. T. Ghasr, D. Simms, and R. Zoughi, "Multimodal solution for a waveguide radiating into multilayered structures—Dielectric property and thickness evaluation," *IEEE Trans. Instrum. Meas.*, vol. 58, no. 5, pp. 1505–1513, May 2009.

[15] T. D. Carrigan *et al.*, "Nondestructive testing of nonmetallic pipelines using microwave reflectometry on an in-line inspection robot," *IEEE Trans. Instrum. Meas.*, vol. 68, no. 2, pp. 586–594, Feb. 2019.

[16] R. J. Stakenborghs, "Microwave inspection method and its application to FRP," in *Proc. MTI AmeriTAC Conf.*, 2013, pp. 1–41.

[17] R. Stakenborghs and J. Little, "Microwave based NDE inspection of HDPE pipe welds," in *Proc. 17th Int. Conf. Nuclear Eng. (ICONE)*, Jan. 2009, pp. 185–193.

[18] K. Schmidt, T. Aljundi, G. A. Subaii, and J. Little, "Microwave interference scanning inspection of nonmetallic pipes," in *Proc. 5th Middle East Nondestruct. Test. Conf. Exhib.*, Manama, Bahrain, 2009, pp. 1–15.

[19] D. M. Tripathi, S. Gunasekaran, S. S. Murugan, and N. A. Enezi, "NDT by microwave test method for non-metallic component," in *Indian National Seminar & Exhibition on Non-Destructive Evaluation NDE*. Thiruvananthapuram, India: Indian National Seminar & Exhibition on Non-Destructive Evaluation NDE, Dec. 2016, pp. 1–7.

[20] M. T. Ghasr, K. Ying, and R. Zoughi, "3D millimeter wave imaging of vertical cracks and its application for the inspection of HDPE pipes," in *Proc. AIP Conf.*, 2014, vol. 1581, no. 1, pp. 1531–1536.

[21] J. Laviada, B. Wu, M. T. Ghasr, and R. Zoughi, "Nondestructive evaluation of microwave-penetrable pipes by synthetic aperture imaging enhanced by full-wave field propagation model," *IEEE Trans. Instrum. Meas.*, vol. 68, no. 4, pp. 1112–1119, Apr. 2019.

[22] B. Wu, Y. Gao, J. Laviada, M. T. Ghasr, and R. Zoughi, "Time-reversal SAR imaging for nondestructive testing of circular and cylindrical multilayered dielectric structures," *IEEE Trans. Instrum. Meas.*, vol. 69, no. 5, pp. 2057–2066, May 2019.

[23] M. D. Buhari, G. Y. Tian, and R. Tiwari, "Microwave-based SAR technique for pipeline inspection using autofocus range-doppler algorithm," *IEEE Sensors J.*, vol. 19, no. 5, pp. 1777–1787, Mar. 2019.

[24] D. M. Sheen, D. L. McMakin, and T. E. Hall, "Three-dimensional millimeter-wave imaging for concealed weapon detection," *IEEE Trans. Microw. Theory Techn.*, vol. 49, no. 9, pp. 1581–1592, Sep. 2001.

[25] M. Ravan, R. K. Amineh, and N. K. Nikolova, "Two-dimensional near-field microwave holography," *Inverse Problems*, vol. 26, no. 5, May 2010, Art. no. 055011.

[26] R. K. Amineh, M. Ravan, A. Khalatpour, and N. K. Nikolova, "Three-dimensional near-field microwave holography using reflected and transmitted signals," *IEEE Trans. Antennas Propag.*, vol. 59, no. 12, pp. 4777–4789, Dec. 2011.

[27] R. K. Amineh, A. Khalatpour, H. Xu, Y. Baskharoun, and N. K. Nikolova, "Three-dimensional near-field microwave holography for tissue imaging," *Int. J. Biomed. Imag.*, vol. 2012, Jan. 2012, Art. no. 291494.

[28] R. K. Amineh, M. Ravan, J. McCombe, and N. K. Nikolova, "Three-dimensional microwave holographic imaging employing forward-scattered waves only," *Int. J. Antennas Propag.*, vol. 2013, pp. 1–15, Jul. 2013.

[29] R. K. Amineh, J. J. McCombe, A. Khalatpour, and N. K. Nikolova, "Microwave holography using point-spread functions measured with calibration objects," *IEEE Trans. Instrum. Meas.*, vol. 64, no. 2, pp. 403–417, Feb. 2015.
[30] R. K. Amineh, N. K. Nikolova, and M. Ravan, *Real-Time Three-Dimensional Imaging of Dielectric Bodies Using Microwave/Millimeter Wave Holography*. Hoboken, NJ, USA: Wiley, 2019.
[31] H. Wu, M. Ravan, R. Sharma, J. Patel, and R. K. Amineh, "Microwave holographic imaging of nonmetallic concentric pipes," *IEEE Trans. Instrum. Meas.*, vol. 69, no. 10, pp. 7594–7605, Oct. 2020.
[32] M. B. Shah, Y. Gao, M. Ravan, and R. K. Amineh, "Thickness profile estimation of fluid-carrying non-metallic pipes," in *Proc. IEEE Int. Microw. Symp. (IMS)*, Jun. 2022, pp. 1–4.
[33] R. K. Amineh, M. Ravan, R. Sharma, and S. Baua, "Three-dimensional holographic imaging using single frequency microwave data," *Int. J. Antennas Propag.*, vol. 2018, pp. 1–14, Jul. 2018.
[34] A. V. Oppenheim, R. W. Schafer, and J. R. Buck, *Discrete-Time Signal Processing*, 2nd ed. Hoboken, NJ, USA: Prentice-Hall, 1999, ISBN: 0137549202.
[35] P. M. Meaney, C. J. Fox, S. D. Geimer, and K. D. Paulsen, "Electrical characterization of glycerin: Water mixtures: Implications for use as a coupling medium in microwave tomography," *IEEE Trans. Microw. Theory Techn.*, vol. 65, no. 5, pp. 1471–1478, May 2017.
[36] TAOGLAS. *White 2.4 / 5.8 GHz Dual Band 3-3.5dBi Rubber Duck Dipole Antenna with RP-SMA(M)*. Accessed: Mar. 1, 2022. [Online]. Available: https://cdn3.taoglas.com/datasheets/GW.48.A151W.pdf
[37] H. Wu, M. Ravan, and R. K. Amineh, "Holographic near-field microwave imaging with antenna arrays in a cylindrical setup," *IEEE Trans. Microw. Theory Techn.*, vol. 69, no. 1, pp. 418–430, Jan. 2021.
[38] H. Wu and R. K. Amineh, "A low-cost and compact three-dimensional microwave holographic imaging system," *Electronics*, vol. 8, no. 9, p. 1036, Sep. 2019.

Maharshi B. Shah (Graduate Student Member, IEEE) received the M.Sc. degree in electrical and computer engineering from the New York Institute of Technology (New York Tech), New York, NY, USA, in 2014, where he is currently pursuing the Ph.D. degree in electrical engineering.

He is a Research Assistant with the Applied Electromagnetics Research Laboratory, New York Tech. His research interests include nondestructive testing, microwave holographic imaging techniques, optimization, and microwave circuit design.

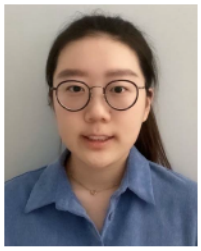

Yuki Gao (Member, IEEE) received the B.S. degree (*summa cum laude*) in electrical and computer engineering from the New York Institute of Technology (New York Tech), New York, NY, USA, in 2021, where she is currently pursuing the M.Sc. degree in electrical and computer engineering under the accelerated program.

She has been a Research Assistant with the Applied Electromagnetics Research Laboratory, New York Tech, since 2019. Her research interests include nondestructive testing, microwave holographic imaging, and microwave sensing.

Ms. Gao was awarded the Microwave Theory and Techniques Society (MTT-S) Undergraduate/Pre-Graduate Scholarship-2022 Cycle 1.

Maryam Ravan (Senior Member, IEEE) received the Ph.D. degree from the Amirkabir University of Technology, Tehran, Iran, in 2007.

She was a Post-Doctoral Fellow with the Departments of Electrical and Computer Engineering, University of Toronto, Toronto, ON, Canada, McMaster University, Hamilton, ON, Canada, and Ryerson University, Toronto, ON, Canada, from 2007 to 2013, where she was involved in solving forward modeling and inverse problems and the related signal/image processing techniques for biomedical, radar systems, microwave imaging, and nondestructive testing (NDT) applications. She was also a Lecturer with the School of Computational Engineering and Science, McMaster University, from 2009 to 2012. From 2013 to 2017, she was a Senior Research Scientist with LivaNova PLC, London, U.K., where her work focused on developing machine learning algorithms for investigating the efficacy of closed-loop vagus nerve stimulation (VNS) therapy for epilepsy. She is currently an Assistant Professor with the Department of Electrical and Computer Engineering, New York Institute of Technology, New York, NY, USA. She has authored over 70 journal and conference papers, a book chapter, and a book. Her research interests include signal and image processing, beamforming, machine learning, microwave holography, multiple input multiple output (MIMO) radar systems and space time adaptive processing, and nondestructive testing. Her research has been supported by the U.S. National Science Foundation, the Department of National Defense/National Science and Engineering Research Council (DND/NSERC) Research Partnership Grant with Defense Research and Development Canada, Ottawa, ON, Canada, and Raytheon Canada Ltd., Ottawa, ON, the Mathematics of Information Technology and Complex System (MITACS) Internship with St. Joseph's Hospital, Hamilton, ON, and the NSERC Engage Grant with Raytheon Canada Ltd.

Reza K. Amineh (Senior Member, IEEE) received the Ph.D. degree in electrical engineering from McMaster University, Hamilton, ON, Canada, in 2010.

He was a Ph.D. Intern with the Advanced Technology Group, BlackBerry, Waterloo, ON, Canada, in 2009. He was a Post-Doctoral Fellow with the University of Toronto, Toronto, Canada, and McMaster University from 2010 to 2013. He was a Principal Scientist with the Department of Sensor Physics, Halliburton Company, Houston, TX, USA. He is currently an Assistant Professor with the Department of Electrical and Computer Engineering, New York Institute of Technology, New York, NY, USA. He has authored/coauthored over 80 journal and conference papers, two book chapters, and a book published by Wiley, New York, NY, and the IEEE Press, Piscataway, NJ, USA. He contributed to more than 40 patent disclosures in applied electromagnetics while working at Halliburton Company. His research interests include applied electromagnetics with applications in imaging and sensing.

Dr. Amineh received several industrial awards. He was a recipient of the Banting Post-Doctoral Fellowship, Canada, in 2012, and the Ontario Ministry of Research and Innovation (OMRI) Post-Doctoral Fellowship in 2010. He has coauthored a paper selected as a finalist in the student paper competition at the IEEE Wireless and Microwave Technology Conference in 2019, an Honorable Mention Paper presented at the IEEE Symposium on Antennas and Propagation in 2008, and a paper selected among the journal of *Inverse Problems*' Highlights Collection of 2010.